Efficient Experimental Verification of Quantum Gates with Local Operations

Rui-Qi Zhang,[1, 2, *] Zhibo Hou,[1, 2, *] Jun-Feng Tang,[1, 2] Jiangwei Shang,[3, †]
Huangjun Zhu,[4, 5, 6, ‡] Guo-Yong Xiang,[1, 2, §] Chuan-Feng Li,[1, 2] and Guang-Can Guo[1, 2]

[1]*Key Laboratory of Quantum Information,University of Science and Technology of China, CAS, Hefei 230026, P. R. China*
[2]*Synergetic Innovation Center of Quantum Information and Quantum Physics,*
University of Science and Technology of China, Hefei 230026, P. R. China
[3]*Key Laboratory of Advanced Optoelectronic Quantum Architecture and Measurement of Ministry of Education,*
School of Physics, Beijing Institute of Technology, Beijing 100081, China
[4]*State Key Laboratory of Surface Physics and Department of Physics, Fudan University, Shanghai 200433, China*
[5]*Institute for Nanoelectronic Devices and Quantum Computing, Fudan University, Shanghai 200433, China*
[6]*Center for Field Theory and Particle Physics, Fudan University, Shanghai 200433, China*
(Dated: July 7, 2021)

Verifying the correct functioning of quantum gates is a crucial step towards reliable quantum information processing, but it becomes an overwhelming challenge as the system size grows due to the dimensionality curse. Recent theoretical breakthroughs show that it is possible to verify various important quantum gates with the optimal sample complexity of $O(1/\epsilon)$ using local operations only, where ϵ is the estimation precision. In this work, we propose a variant of quantum gate verification (QGV) which is robust to practical gate imperfections, and experimentally realize efficient QGV on a two-qubit controlled-not gate and a three-qubit Toffoli gate using only local state preparations and measurements. The experimental results show that, by using only 1600 and 2600 measurements on average, we can verify with 95% confidence level that the implemented controlled-not gate and Toffoli gate have fidelities at least 99% and 97%, respectively. Demonstrating the superior low sample complexity and experimental feasibility of QGV, our work promises a solution to the dimensionality curse in verifying large quantum devices in the quantum era.

Introduction.—Quantum computers can perform computational tasks much more efficiently [1, 2] and even exponentially faster than their classical counterparts [3–5]. Before harnessing the power of a quantum computer, a crucial step is to verify the correct functioning of its building blocks, i.e., the quantum gates. Traditional quantum process tomography (QPT) [6, 7] can provide the complete information of a quantum gate and is a feasible solution for small systems. However, QPT is not scalable as its complexity grows exponentially with the size of the quantum system, and so far has been applied to quantum gates acting on no more than three qubits [8–10]. This exponential resource cost cannot be circumvented in general even if one can take advantage of the sparsity of the underlying structures [11–13] or heuristic algorithms [14, 15].

The key observation towards efficient verification of a quantum gate is that the complete information of a quantum gate is usually not necessary in many tasks. Quite often the fidelity of a quantum gate is enough to characterize its quality. Fidelity estimation based on unitary 2-designs and the twirling protocol [16, 17] can estimate the fidelity of a Clifford gate with size-independent sample complexity of $O(1/\epsilon^2)$, where ϵ is the estimation precision. Direct fidelity estimation and Monte Carlo sampling [18–20] can achieve a similar sample complexity for Clifford and other well-conditioned gates even if one can only prepare product states and perform Pauli measurements. Randomized benchmarking (RB) [21–24] can certify Clifford gates and some special non-Clifford gates with a similar sample complexity, and possesses the addi-

tional advantage of robustness against state-preparation and measurement errors.

Despite the progresses mentioned above, most approaches in the literature have disadvantages, which limit their applicability. Notably, most approaches are limited to a few types of quantum gates (say Clifford gates) [16–21]. In addition, they have a suboptimal scaling behavior in the precision ϵ. Moreover, many approaches, including twirling protocols and RB, require entangling operations [16, 17, 21–24], that is, preparing entangled states or performing entangling measurements.

Recently, an alternative approach called quantum gate verification (QGV) or quantum process verification (QPV) [25–27] has been developed to tackle these problems. It is inspired by probabilistic verification protocols which have found fruitful applications in certifying quantum states [28–32] and entanglement [33, 34]. With this approach, a variety of quantum gates can be verified efficiently with the optimal sample complexity of $O(1/\epsilon)$ using only local state preparations and measurements. Nevertheless, the current formulation of QGV can reach a valid conclusion only when the gate to be verified passes all the tests, which may prevent QGV from obtaining a valid conclusion when a realistic quantum gate with acceptable infidelity is considered.

In this Letter, we propose a variant of QGV which is tolerant to gate imperfections, while keeping its efficiency. With this robust proposal, we experimentally apply QGV to a two-qubit controlled-not (CNOT) gate realized in a photonic system. By using 20 experimental settings and 1600 samples on average we can verify that
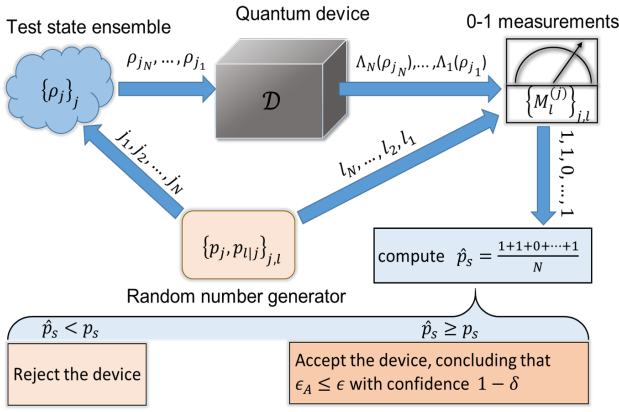
FIG. 1. Procedure for verifying the quantum device $\mathcal{D}$. In each run, the random number generator generates random numbers j and l according to the probabilities p_j and $p_{l|j}$ (conditioned on j), respectively. Then state ρ_j is drawn from the set of test states and sent to $\mathcal{D}$; next, the measurement module implements a two-outcome measurement $\{M_l^{(j)}, \mathbb{1} - M_l^{(j)}\}$ on the output state $\Lambda(\rho_j)$. By repeating the above procedure N times, the verifier can reach a conclusion on the quality of $\mathcal{D}$ based on the passing frequency $\hat{p}_s$ over the N tests.

the CNOT gate has at least 99% fidelity with a 95% confidence level. We then apply QGV to a three-qubit Toffoli gate to illustrate the scalability and superiority of QGV. By using 32 measurement settings and 2600 samples on average we can verify that the fidelity of the Toffoli gate is at least 97% with a 95% confidence level. By contrast, the standard QPT would require at least 4096 measurement settings and over a million measurements in total to characterize the Toffoli gate. Our experiments demonstrate that efficient verification of quantum gates can be achieved with only local state preparations and measurements.

Theoretical framework.—Consider a quantum device that is expected to implement a target unitary transformation $\mathcal{U}$, but actually realizes N unknown quantum channels $\Lambda_1, ..., \Lambda_N$, which are assumed to be identical and independent, over the N runs. In practice, these channels might deviate from $\mathcal{U}$. Let $1 - \epsilon_A$ be the average gate fidelity of the channels with respect to $\mathcal{U}$. Our goal is to verify, with some confidence level $1 - \delta$ (significance level δ), that the average gate infidelity of the channels is not larger than a given threshold ϵ, i.e.,

$$\epsilon_A \leq \epsilon, \quad \text{with confidence level } 1 - \delta. \tag{1}$$

The verification procedure, illustrated in Fig. 1, can be described as follows [26]. In the ith run, the verifier first randomly chooses a pure state $\rho_j = |\psi_j\rangle\langle\psi_j|$ with probability p_j from a set of test states $\{\rho_j\}_j$ and subjects it to the device. Then the verifier performs a two-outcome measurement $\{M_l^{(j)}, \mathbb{1} - M_l^{(j)}\}$, which is called a test, on the output state $\Lambda_i(\rho_j)$ with outcome 1 for passing and

0 for failure. Here the test operator $M_l^{(j)}$ needs to satisfy the condition $\text{Tr}[M_l^{(j)}\mathcal{U}(\rho_j)] = 1$ and is chosen randomly with the conditional probability $p_{l|j}$ from a test set $\{M_l^{(j)}\}_l$ that depends on $\mathcal{U}(\rho_j)$. The verifier records the test results of the N runs and compares the passing rate $\hat{p}_s$ with a given threshold p_s, based on which the device is accepted or rejected.

The performance of the above verification procedure is mainly determined by the *process verification operator* defined as [26]

$$\Theta := d \sum_j p_j \mathcal{U}^{-1}\left(\sum_l p_{l|j} M_l^{(j)}\right) \otimes \rho_j^*. \tag{2}$$

For a perfect device, the acceptance probability is unity. If the quantum gate realized has (average gate) infidelity ϵ, by contrast, the acceptance probability is upper bounded by $[p_A(\Theta, \epsilon)]^N$, where $p_A(\Theta, \epsilon)$ is defined as the maximal passing probability for quantum gates with infidelity $\epsilon_A \geq \epsilon$ given the verification operator Θ [26]. If we set $p_s = 1$, then the minimal number of tests required to verify the quantum gate with infidelity ϵ and confidence level $1 - \delta$ reads

$$N(\epsilon, \delta, \Theta) = \left\lceil \frac{\ln \delta}{\ln p_A(\Theta, \epsilon)} \right\rceil. \tag{3}$$

This number is minimized when the test states ρ_j form a 2-design [35, 36] and the test operator for each test state ρ_j is chosen to be the projector $\mathcal{U}(\rho_j)$ onto the target output state, in which case $p_A(\Theta, \epsilon) = 1 - \epsilon$, and Eq. (3) reduces to [26]

$$N^{\text{opt}}(\epsilon, \delta) = \left\lceil \frac{\ln \delta}{\ln(1 - \epsilon)} \right\rceil \overset{\epsilon \to 0}{\approx} \frac{\ln \delta^{-1}}{\epsilon}. \tag{4}$$

In general, to realize the optimal verification protocol mentioned above would require entangling operations, which are often inaccessible. Fortunately, for many important quantum gates, nearly optimal performance can be achieved using local state preparations and local projective measurements only [25–27]. For simplicity, in this work we focus on verification protocols that are balanced, which means the set of test states satisfies the condition $\sum_j p_j \rho_j = \mathbb{1}/d$, where d is the dimension of the underlying Hilbert space. Denote by $\nu := \nu(\Theta)$ the spectral gap of Θ (between the largest and the second largest eigenvalues), then we have

$$N^{\text{local}}(\epsilon, \delta, \Theta) \leq \left\lceil \frac{\ln \delta}{\ln(1 - \nu\epsilon)} \right\rceil \leq \left\lceil \frac{\ln \delta^{-1}}{\nu\epsilon} \right\rceil. \tag{5}$$

In practice, quantum gates are never perfect. Even if they satisfy the condition $\epsilon_A \leq \epsilon$, a few failure events might happen with a non-negligible probability among the N tests. In this case, setting $p_s = 1$ for the threshold would reject a properly functioning device with certain

probability. To remedy this problem and construct a robust verification protocol, we need to consider the situation with $p_s < 1$. To be concrete, if the passing frequency $\hat{p}_s$ over the N tests is larger than $p_A(\Theta, \epsilon)$, then the confidence level $1 - \delta(\hat{p}_s)$ that the device satisfies $\epsilon_A \leq \epsilon$ is lower bounded by

$$1 - \delta(\hat{p}_s) \geq 1 - e^{-D(\hat{p}_s \| p_A(\Theta, \epsilon))N} , \qquad (6)$$

where $D(x\|y) = x \ln(\frac{x}{y}) + (1-x) \ln(\frac{1-x}{1-y})$ is the Kullback-Leibler divergence. On the other hand, given the confidence level $1 - \delta$, we can derive from Eq. (6) an upper bound for the infidelity ϵ_A,

$$\epsilon_A \leq \frac{d}{d+1} \frac{1 - D^{(-1)}(\hat{p}_s, \ln \delta^{-1}/N)}{\nu(\Theta)} , \qquad (7)$$

where $D^{(-1)}(\hat{p}_s, y)$ is the inverse function of $y = D(\hat{p}_s\|x)$ with domain $0 \leq x < \hat{p}_s$ (for a fixed $\hat{p}_s$). The detailed derivations of Eqs. (6) and (7) are relegated to Sec. S1 in the Supplemental Material [37].

Experimental setup.—The experimental setups for verifying two-qubit and three-qubit quantum gates are shown in Fig. 2. Both of them consist of three modules: a state-preparation module, a quantum-gate module, and a measurement module. Here we use the path and polarization degrees of freedom (DoFs) of the heralded photon to encode the test state employed in the verification. The two-qubit system consists of a path DoF with up and down modes and a polarization DoF with horizontal (H) and vertical (V) polarizations; by contrast, the three-qubit system consists of a path DoF with left-right modes and up-down modes and a polarization DoF.

The heralded single-photon source shown in Fig. 2 is used by both setups. An ultraviolet laser with central wavelength of 404nm is used to pump a type-I phase-matched β-barium-borate (BBO) crystal to generate a photon pair in the product (polarization) state via spontaneous parametric down-conversion [38]. One photon is measured as a trigger to herald the generation of its twin photon, which is then transmitted to the state-preparation module.

The state-preparation module in the two-qubit (three-qubit) setup is designed to prepare arbitrary two-qubit (three-qubit) product states by virtue of photonic quantum walks. Here the coin operators required are realized by combinations of half-wave plates (HWPs) and quarter-wave plates (QWPs); see Sec. S2 of the Supplemental Material [37]. The K9 plates in the state-preparation module in the three-qubit setup are used to compensate for the path-length difference among the interference arms.

The quantum-gate module implements the quantum gate to be verified, which can be seen as a black box that is expected to perform the target unitary transformation on the input quantum states. The measurement module in the two-qubit (three-qubit) setup is designed to realize arbitrary local projective measurements on two-qubit

(three-qubit) systems by using photonic quantum walks. The QWP-HWP pairs inside the measurement module control the measurement settings for individual qubits; see Sec. S2 of the Supplemental Material [37]. In addition, the K9 plates are used to compensate for the path-length difference among the interference arms. Finally, the heralded photon is collected by two polarization analyzing systems (PASs) in the two-qubit setup and four PASs in the three-qubit setup, where the PASs measure the polarization of the input photon in the $\{|H\rangle, |V\rangle\}$ basis.

Results.—To demonstrate the efficiency and scalability of QGV, we performed QGV on a two-qubit CNOT gate and a three-qubit Toffoli gate. The CNOT gate (Toffoli gate) is implemented by inserting a HWP with its optical axis aligned at $45°$ to the horizontal direction on path 1 (11) in the two-qubit (three-qubit) setup. The sets of test states and measurement settings employed for verifying the CNOT gate and Toffoli gate are detailed in Sec. S3 of the Supplemental Material [37].

The performance of QGV is characterized by the scalings of the significance level δ and infidelity ϵ_A with respect to the number of tests N. The values of δ and ϵ_A after each test can be determined from the test results by virtue of Eqs. (6) and (7). Since the results of a single run of QGV suffer from statistical fluctuations, which would prevent us from reliably evaluating the performance, we repeat the verification procedure 50 times under the same conditions (e.g., the set of test states and the number of tests in total). The average values of δ and ϵ_A are calculated by substituting $\hat{p}_s$ in Eqs. (6) and (7) with $\sum_{i=1}^{50} \hat{p}_s^{(i)}/50$ for each value of N, where $\hat{p}_s^{(i)}$ is the passing rate of the ith run among the first N tests. We also use Eqs. (6) and (7) to fit the average results by fixing the value of $\hat{p}_s$ to be the average passing rate over the 50 runs of QGV among all the tests used.

The experimental results on the verification of the CNOT gate are shown in Fig. 3, where 20 different measurement settings and 6000 tests in total (see Sec. S3 of the Supplemental Material [37] for details) are used in each run of QGV. In Fig. 3(a), where ϵ is set to be 0.01, δ rapidly drops below 0.05 within 1600 tests for both the single-run and average results, which means that the CNOT gate is verified efficiently with high confidence level. Alternatively, we can set the confidence level $1 - \delta$ to be 0.95 and calculate ϵ_A. Fig. 3(b) shows that ϵ_A descends below 0.01 after 1600 tests for both the single-run and average results, which is consistent with Fig. 3(a). The scaling of the average infidelity ϵ_A with respect to N can be described by the power law $N^{-0.857}$ within the first 200 tests, which is quite close to the optimal scaling of N^{-1} in Eq. (4). After 200 tests the descending speed of ϵ_A gradually slows down as it gets closer to the actual infidelity, and eventually converges to 0.0045 after 10000 tests (see Sec. S4 of the Supplemental Material [37]). In both Fig. 3(a) and (b), the single-run results break up
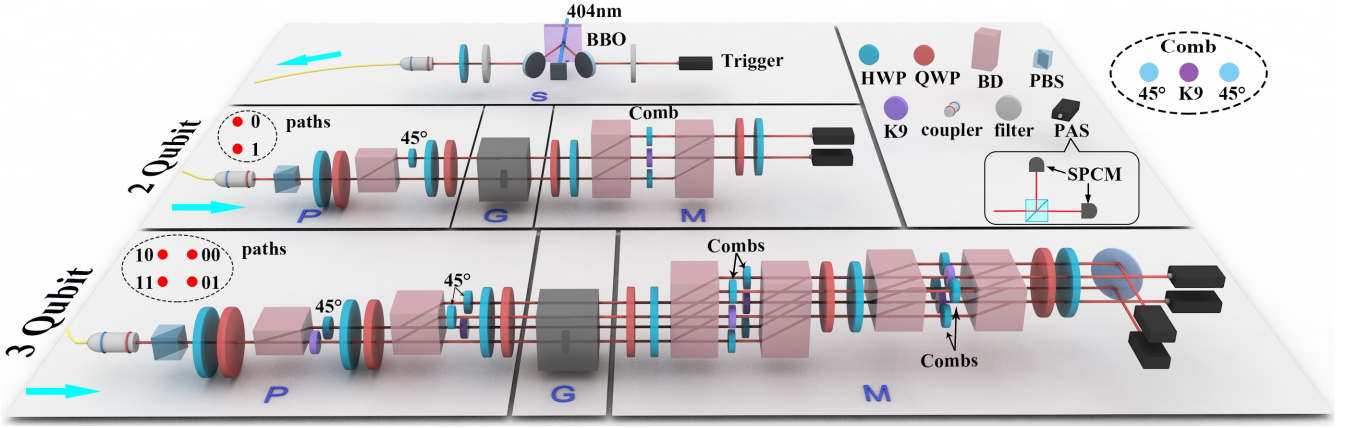
FIG. 2. Experimental setup. The heralded single-photon source (labeled by S) is realized by spontaneous parametric down-conversion in a type-I β-barium-borate (BBO) crystal. The figure shows two independent setups employed for implementing the verification protocols for the two-qubit CNOT gate and three-qubit Toffoli gate, respectively. Each setup consists of three modules: a state-preparation module (labeled by P), a quantum-gate module (labeled by G), and a measurement module (labeled by M). The inset in the component panel (upper right) shows the details of the polarization analyzing system (PAS). Each PAS consists of one polarizing beam-splitter (PBS) and two single-photon counting modules (SPCMs) and can measure the photons in the $\{|H\rangle, |V\rangle\}$ polarization basis. HWP: half-wave plate; QWP: quarter-wave plate; BD: beam displacer; K9: K9 plate.
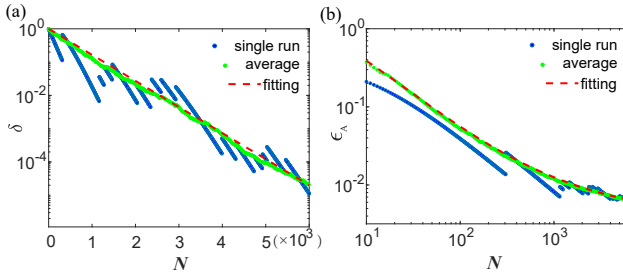
FIG. 3. Experimental results on the verification of the CNOT gate. The blue dots represent the results of a single run of QGV. The green dots represent the average results of 50 runs of QGV. The red dotted line is the fitting line for the average results. (a) When ϵ is set to 0.01, δ is log plotted versus N. (b) When δ is set to 0.05, ϵ_A is log-log plotted versus N. Within the first 200 tests, the scaling of ϵ_A averaged over 50 runs with respect to N is fitted to be $N^{-0.857}$ by linear regression.

FIG. 4. Experimental results on the verification of the Toffoli gate. The meanings of the data points are similar to those in Fig. 3. (a) When ϵ is set to 0.03, δ is log plotted versus N. (b) When δ is set to 0.05, ϵ_A is log-log plotted versus N. Within the first 200 tests, the scaling of ϵ_A averaged over 50 runs with respect to N is fitted to be $N^{-0.840}$ by linear regression.

into discrete short segments due to the occasional failures caused by the deviation of the actual gate from the ideal target gate.

We then perform QPT on the CNOT gate and find that the actual average gate fidelity is 99.7%, which is consistent with the QGV result. To perform QPT on the CNOT gate, we employ 36 product Pauli eigenstates as the test states and 9 measurement settings based on Pauli measurements for each output state. The experimental details are relegated to Sec. S5 of the Supplemental Material [37]. Here the total number of experimental settings is 324, and the total number of measurements is over 6 million, which are substantially more than that required in QGV (the number of measurements in QPT can be re-

duced, but the conclusion does not change). These facts clearly reflect the advantage of QGV over QPT.

To demonstrate the scalability of QGV, next we consider the verification of the three-qubit Toffoli gate. In this case, 32 different experimental settings and 10000 tests in total are employed in each run of QGV (see Sec. S3 of the Supplemental Material [37] for details). The verification results are shown in Fig. 4, which are analogous to the counterparts shown in Fig. 3. To verify the Toffoli gate within infidelity 0.03 and confidence level 95%, only 2600 tests are required. In Fig. 4(b), ϵ_A exhibits $N^{-0.840}$ scaling with respect to N within the first 200 tests, which is also close to the optimal scaling of N^{-1}. The infidelity estimator ϵ_A eventually converges to 0.0148 after 40000 tests; see Sec. S4 of the Supplemen-

tal Material [37]. In both plots in Fig. 4, the single-run results break up more frequently than their counterparts in Fig. 3, due to the larger deviation of the actual Toffoli gate from the ideal Toffoli gate. Incidentally, to perform QPT on the Toffoli gate would require $8^4 = 4096$ experimental settings and millions of measurements in total, which are quite prohibitive and much more resource consuming than QGV.

Summary.—By virtue of photonic systems, we experimentally realized efficient verification of a CNOT gate and a Toffoli gate with local state preparations and measurements. The experimental results clearly show that the verification protocols can achieve nearly optimal performance without relying on entangling operations, and are substantially more efficient than QPT. Moreover, they are scalable and robust to the imperfections of the actual quantum gates. Notably, only 2600 tests are required to verify the Toffoli gate with fidelity 97% and confidence level 95%. Our work demonstrates that QGV is a powerful tool for the verification of quantum gates and quantum devices, and may play a key role in the development of quantum technologies.

* These authors contributed equally to this work.
† jiangwei.shang@bit.edu.cn
‡ zhuhuangjun@fudan.edu.cn
§ gyxiang@ustc.edu.cn

[1] A. W. Harrow, A. Hassidim, and S. Lloyd, Phys. Rev. Lett. **103**, 150502 (2009).
[2] L. K. Grover, in *Proceedings of the Twenty-Eighth Annual ACM Symposium on Theory of Computing*, STOC '96 (Association for Computing Machinery, New York, NY, USA, 1996) p. 212–219.
[3] P. Shor, in *Proceedings of the 35th Annual Symposium on Foundations of Computer Science* (1994) pp. 124–134.
[4] S. Aaronson and A. Arkhipov, in *Proceedings of the Forty-Third Annual ACM Symposium on Theory of Computing*, STOC '11 (Association for Computing Machinery, New York, NY, USA, 2011) p. 333–342.
[5] H.-S. Zhong, H. Wang, Y.-H. Deng, M.-C. Chen, L.-C. Peng, Y.-H. Luo, J. Qin, D. Wu, X. Ding, Y. Hu, P. Hu, X.-Y. Yang, W.-J. Zhang, H. Li, Y. Li, X. Jiang, L. Gan, G. Yang, L. You, Z. Wang, L. Li, N.-L. Liu, C.-Y. Lu, and J.-W. Pan, Science **370**, 1460 (2020).
[6] I. L. Chuang and M. A. Nielsen, J. Mod. Opt. **44**, 2455 (1997).
[7] J. F. Poyatos, J. I. Cirac, and P. Zoller, Phys. Rev. Lett. **78**, 390 (1997).
[8] M. Riebe, K. Kim, P. Schindler, T. Monz, P. O. Schmidt, T. K. Körber, W. Hänsel, H. Häffner, C. F. Roos, and R. Blatt, Phys. Rev. Lett. **97**, 220407 (2006).
[9] R. C. Bialczak, M. Ansmann, M. Hofheinz, E. Lucero, M. Neeley, A. D. O'Connell, D. Sank, H. Wang, J. Wenner, M. Steffen, A. N. Cleland, and J. M. Martinis, Nat. Phys. **6**, 409 (2010).
[10] Y. S. Weinstein, T. F. Havel, J. Emerson, N. Boulant, M. Saraceno, S. Lloyd, and D. G. Cory, J. Chem. Phys. **121**, 6117 (2004).
[11] D. Gross, Y.-K. Liu, S. T. Flammia, S. Becker, and J. Eisert, Phys. Rev. Lett. **105**, 150401 (2010).
[12] S. T. Flammia, D. Gross, Y.-K. Liu, and J. Eisert, New J. Phys. **14**, 095022 (2012).
[13] M. Cramer, M. B. Plenio, S. T. Flammia, R. Somma, D. Gross, S. D. Bartlett, O. Landon-Cardinal, D. Poulin, and Y.-K. Liu, Nat. Commun. **1**, 149 (2010).
[14] C. Ferrie, Phys. Rev. Lett. **113**, 190404 (2014).
[15] Z. Hou, J.-F. Tang, C. Ferrie, G.-Y. Xiang, C.-F. Li, and G.-C. Guo, Phys. Rev. A **101**, 022317 (2020).
[16] C. Dankert, R. Cleve, J. Emerson, and E. Livine, Phys. Rev. A **80**, 012304 (2009).
[17] D. Lu, H. Li, D.-A. Trottier, J. Li, A. Brodutch, A. P. Krismanich, A. Ghavami, G. I. Dmitrienko, G. Long, J. Baugh, and R. Laflamme, Phys. Rev. Lett. **114**, 140505 (2015).
[18] S. T. Flammia and Y.-K. Liu, Phys. Rev. Lett. **106**, 230501 (2011).
[19] M. P. da Silva, O. Landon-Cardinal, and D. Poulin, Phys. Rev. Lett. **107**, 210404 (2011).
[20] L. Steffen, M. P. da Silva, A. Fedorov, M. Baur, and A. Wallraff, Phys. Rev. Lett. **108**, 260506 (2012).
[21] E. Magesan, J. M. Gambetta, B. R. Johnson, C. A. Ryan, J. M. Chow, S. T. Merkel, M. P. da Silva, G. A. Keefe, M. B. Rothwell, T. A. Ohki, M. B. Ketchen, and M. Steffen, Phys. Rev. Lett. **109**, 080505 (2012).
[22] R. Harper and S. T. Flammia, Quantum Sci. Technol. **2**, 015008 (2017).
[23] E. Onorati, A. H. Werner, and J. Eisert, Phys. Rev. Lett. **123**, 060501 (2019).
[24] S. Garion, N. Kanazawa, H. Landa, D. C. McKay, S. Sheldon, A. W. Cross, and C. J. Wood, Phys. Rev. Research **3**, 013204 (2021).
[25] Y.-C. Liu, J. Shang, X.-D. Yu, and X. Zhang, Phys. Rev. A **101**, 042315 (2020).
[26] H. Zhu and H. Zhang, Phys. Rev. A **101**, 042316 (2020).
[27] P. Zeng, Y. Zhou, and Z. Liu, Phys. Rev. Research **2**, 023306 (2020).
[28] M. Hayashi, K. Matsumoto, and Y. Tsuda, J. Phys. A: Math. Gen. **39**, 14427 (2006).

[29] S. Pallister, N. Linden, and A. Montanaro, Phys. Rev. Lett. **120**, 170502 (2018).

[30] W.-H. Zhang, C. Zhang, Z. Chen, X.-X. Peng, X.-Y. Xu, P. Yin, S. Yu, X.-J. Ye, Y.-J. Han, J.-S. Xu, G. Chen, C.-F. Li, and G.-C. Guo, Phys. Rev. Lett. **125**, 030506 (2020).

[31] H. Zhu and M. Hayashi, Phys. Rev. Lett. **123**, 260504 (2019).

[32] Y.-C. Liu, J. Shang, R. Han, and X. Zhang, Phys. Rev. Lett. **126**, 090504 (2021).

[33] A. Dimić and B. Dakić, npj Quantum Inf. **4**, 11 (2018).

[34] V. Saggio, A. Dimić, C. Greganti, L. A. Rozema, P. Walther, and B. Dakić, Nat. Phys. **15**, 935 (2019).

[35] J. M. Renes, R. Blume-Kohout, A. J. Scott, and C. M. Caves, J. Math. Phys. **45**, 2171 (2004).

[36] A. Roy and A. J. Scott, J. Math. Phys. **48**, 072110 (2007).

[37] See Supplemental Material for the details.

[38] P. G. Kwiat, E. Waks, A. G. White, I. Appelbaum, and P. H. Eberhard, Phys. Rev. A **60**, R773 (1999).

Efficient Experimental Verification of Quantum Gates with Local Operations: Supplemental Material

Rui-Qi Zhang,[1, 2, *] Zhibo Hou,[1, 2, *] Jun-Feng Tang,[1, 2] Jiangwei Shang,[3, †]
Huangjun Zhu,[4, 5, 6, ‡] Guo-Yong Xiang,[1, 2, §] Chuan-Feng Li,[1, 2] and Guang-Can Guo[1, 2]

[1]*Key Laboratory of Quantum Information,*
University of Science and Technology of China, CAS, Hefei 230026, P. R. China
[2]*Synergetic Innovation Center of Quantum Information and Quantum Physics,*
University of Science and Technology of China, Hefei 230026, P. R. China
[3]*Key Laboratory of Advanced Optoelectronic Quantum Architecture*
and Measurement of Ministry of Education, School of Physics,
Beijing Institute of Technology, Beijing 100081, China
[4]*State Key Laboratory of Surface Physics and Department of Physics,*
Fudan University, Shanghai 200433, China
[5]*Institute for Nanoelectronic Devices and Quantum Computing,*
Fudan University, Shanghai 200433, China
[6]*Center for Field Theory and Particle Physics,*
Fudan University, Shanghai 200433, China
(Dated: July 7, 2021)

S1. ESTIMATION OF THE CONFIDENCE LEVEL AND INFIDELITY FROM TEST RESULTS

In this section we prove Eqs. (6) and (7) in the main text. Recall that $p_A(\Theta, \epsilon)$ is the maximal passing probability for quantum gates with infidelity $\epsilon_A \geq \epsilon$ given the process verification operator Θ [1]. By definition, $p_A(\Theta, \epsilon)$ is nonincreasing in ϵ. Note that the passing probability is upper bounded by $p_A(\Theta, \epsilon)$ whenever the quantum gate under consideration has infidelity $\epsilon_A \geq \epsilon$. Let $\hat{p}_s$ be the passing rate of a quantum gate in a given experiment with N tests. The significance level $\delta(\hat{p}_s)$ that the infidelity satisfies $\epsilon_A < \epsilon$ is defined as the maximal probability that the passing rate is larger than $\hat{p}_s$ for any quantum gate that satisfies $\epsilon_A \geq \epsilon$. If $\hat{p}_s > p_A(\Theta, \epsilon)$, then the Chernoff bound [2] implies that

$$\delta(\hat{p}_s) \leq \exp[-D(\hat{p}_s \| p_A(\Theta, \epsilon))N], \tag{S1}$$

which is equivalent to Eq. (6) in the main text.

To prove Eq. (7) in the main text, note that, for a balanced verification strategy Θ, the probability $p_A(\Theta, \epsilon)$ satisfies [1]

$$p_A(\Theta, \epsilon) \leq 1 - \frac{d+1}{d}\nu(\Theta)\epsilon, \tag{S2}$$

where $\nu(\Theta)$ is the spectral gap of Θ, that is, the gap between the largest eigenvalue of Θ (which is unity) and the second largest eigenvalue of Θ. The above equation implies that

$$\epsilon \leq \frac{d}{d+1}\frac{1 - p_A(\Theta, \epsilon)}{\nu(\Theta)}, \tag{S3}$$

which sets an upper bound for the infidelity given the maximal passing probability $p_A(\Theta, \epsilon)$. Now we rearrange Eq. (S1) to derive

$$p_A(\Theta, \epsilon) \geq D^{(-1)}\left(\hat{p}_s, \frac{\ln \delta^{-1}}{N}\right), \tag{S4}$$

where $x = D^{(-1)}(\hat{p}_s, y)$ is the inverse function of $y = D(\hat{p}_s \| x)$ with domain $x \in (0, \hat{p}_s]$. Note that $D(\hat{p}_s \| x)$ is strictly decreasing in $x \in (0, \hat{p}_s]$, so $D^{(-1)}(\hat{p}_s, y)$ is well defined for $y \geq 0$. Combining Eqs. (S3) and (S4), we can deduce that

$$\epsilon_A \leq \frac{d}{d+1}\frac{1 - D^{(-1)}\left(\hat{p}_s, \frac{\ln \delta^{-1}}{N}\right)}{\nu(\Theta)}, \tag{S5}$$

which confirms Eq. (7) in the main text.

S2. EXPERIMENTAL IMPLEMENTATIONS

In this section we show that the two state-preparation modules in Fig. 2 in the main text can prepare arbitrary product states of two- and three-qubit systems, respectively. In addition, the two measurement modules in Fig. 2 can perform arbitrary local projective measurements on two- and three-qubit systems, respectively.
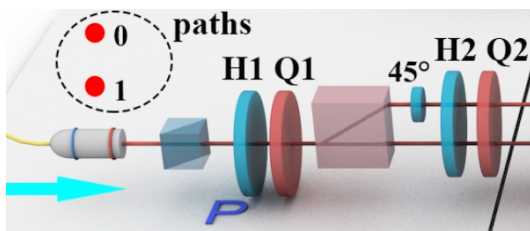
FIG. S1. The state-preparation module for the verification of the CNOT gate.

A. Preparation of two-qubit product states

The state-preparation module for the verification of the CNOT gate is reproduced in Fig. S1. Suppose the angles of the optical axes of H1, Q1, H2, and Q2 in the figure are h_1, q_1, h_2, and q_2 (with respect to the horizontal direction), respectively. The input heralded photon is initially prepared in the state $|1\rangle \otimes |H\rangle$, which is transformed into the following state

$$|1\rangle \otimes \big[\cos(q_1)\cos(q_1 - 2h_1) + \mathrm{i}\sin(q_1)\sin(q_1 - 2h_1)\big]|H\rangle$$
$$+|1\rangle \otimes \big[\sin(q_1)\cos(q_1 - 2h_1) - \mathrm{i}\cos(q_1)\sin(q_1 - 2h_1)\big]|V\rangle \tag{S6}$$

by H1 and Q1. The BD after Q1 coherently routes the heralded photon to paths 0 and 1 according to the polarization state of the heralded photon, which yields the state

$$|0\rangle \otimes \big[\sin(q_1)\cos(q_1 - 2h_1) - \mathrm{i}\cos(q_1)\sin(q_1 - 2h_1)\big]|V\rangle$$
$$+|1\rangle \otimes \big[\cos(q_1)\cos(q_1 - 2h_1) + \mathrm{i}\sin(q_1)\sin(q_1 - 2h_1)\big]|H\rangle . \tag{S7}$$

Then H2 and Q3 together with a 45° HWP transform the photon state into

$$(a_0|0\rangle + a_1|1\rangle) \otimes (b_0|H\rangle + b_1|V\rangle) , \tag{S8}$$

where

$$a_0 := \sin(q_1)\cos(q_1 - 2h_1) - \mathrm{i}\cos(q_1)\sin(q_1 - 2h_1) ,$$
$$a_1 := \cos(q_1)\cos(q_1 - 2h_1) + \mathrm{i}\sin(q_1)\sin(q_1 - 2h_1) ,$$
$$b_0 := \cos(q_2)\cos(q_2 - 2h_2) + \mathrm{i}\sin(q_2)\sin(q_2 - 2h_2) ,$$
$$b_1 := \sin(q_2)\cos(q_2 - 2h_2) - \mathrm{i}\cos(q_2)\sin(q_2 - 2h_2) . \tag{S9}$$

Hence, to prepare the state in Eq. (8) in the main text, we need to choose appropriate values of the parameters h_1, q_1, h_2, and q_2 to satisfy the conditions in Eq. (S9).

B. Preparation of three-qubit product states

The state-preparation module for the verification of the Toffoli gate is reproduced in Fig. S2. Suppose the angles of the optical axes of H1, Q1, H2, Q2, H3, and Q3 in the figure are h_1, q_1, h_2, q_2, h_3, and q_3 (with respect to the horizontal direction), respectively. The input heralded photon is initially prepared in the state $|11\rangle \otimes |H\rangle$, which is turned into the following state

$$|11\rangle \otimes \big[\cos(q_1)\cos(q_1 - 2h_1) + \mathrm{i}\sin(q_1)\sin(q_1 - 2h_1)\big]|H\rangle$$
$$+|11\rangle \otimes \big[\sin(q_1)\cos(q_1 - 2h_1) - \mathrm{i}\cos(q_1)\sin(q_1 - 2h_1)\big]|V\rangle \tag{S10}$$
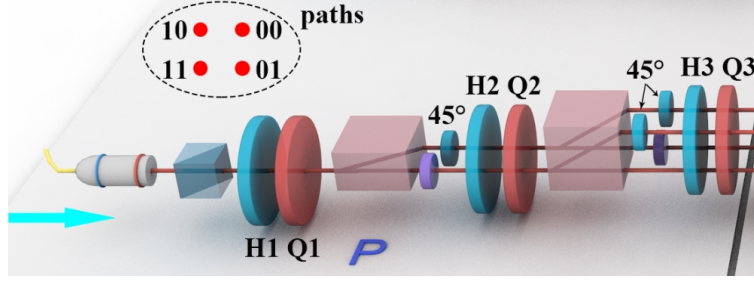
FIG. S2. The state-preparation module for the verification of the Toffoli gate.

by H1 and Q1. The BD after Q1 coherently routes the heralded photon to paths 11 and 01 according to the polarization state of the heralded photon, which yields the state

$$|01\rangle \otimes \big[\sin(q_1)\cos(q_1 - 2h_1) - \mathrm{i}\cos(q_1)\sin(q_1 - 2h_1)\big]|V\rangle$$
$$+|11\rangle \otimes \big[\cos(q_1)\cos(q_1 - 2h_1) + \mathrm{i}\sin(q_1)\sin(q_1 - 2h_1)\big]|H\rangle. \tag{S11}$$

Then a 45° HWP (which flips the photon's polarization) together with a K9 plate (which compensates the path-length difference) transforms the photon state into

$$(a_0'|0\rangle + a_1'|1\rangle) \otimes |1\rangle \otimes |H\rangle, \tag{S12}$$

where

$$a_0' := \sin(q_1)\cos(q_1 - 2h_1) - \mathrm{i}\cos(q_1)\sin(q_1 - 2h_1),$$
$$a_1' := \cos(q_1)\cos(q_1 - 2h_1) + \mathrm{i}\sin(q_1)\sin(q_1 - 2h_1). \tag{S13}$$

This initializes the first qubit.

Next, H2 and Q2 transform the photon state into

$$(a_0'|0\rangle + a_1'|1\rangle) \otimes |1\rangle \otimes \big\{ [\cos(q_2)\cos(q_2 - 2h_2) + \mathrm{i}\sin(q_2)\sin(q_2 - 2h_2)]|H\rangle$$
$$+ [\sin(q_2)\cos(q_2 - 2h_2) - \mathrm{i}\cos(q_2)\sin(q_2 - 2h_2)]|V\rangle \big\}. \tag{S14}$$

Then the second BD together with two 45° HWPs and a K9 plate transform the state of the heralded photon into

$$(a_0'|0\rangle + a_1'|1\rangle) \otimes (b_0'|0\rangle + b_1'|1\rangle) \otimes |H\rangle, \tag{S15}$$

where

$$b_0' := \sin(q_2)\cos(q_2 - 2h_2) - \mathrm{i}\cos(q_2)\sin(q_2 - 2h_2),$$
$$b_1' := \cos(q_2)\cos(q_2 - 2h_2) + \mathrm{i}\sin(q_2)\sin(q_2 - 2h_2). \tag{S16}$$

This initializes the second qubit.

Finally, H3 and Q3 transform the photon state into

$$(a_0'|0\rangle + a_1'|1\rangle) \otimes (b_0'|0\rangle + b_1'|1\rangle) \otimes (c_0'|H\rangle + c_1'|V\rangle), \tag{S17}$$

where

$$c_0' := \sin(q_3)\cos(q_3 - 2h_3) - \mathrm{i}\cos(q_3)\sin(q_3 - 2h_3),$$
$$c_1' := \cos(q_3)\cos(q_3 - 2h_3) + \mathrm{i}\sin(q_3)\sin(q_3 - 2h_3). \tag{S18}$$

This initializes the third qubit. Hence, to prepare the state in Eq. (9) in the main text, we need to choose proper values of the parameters h_1, q_1, h_2, q_2, h_3, and q_3 to satisfy the conditions in Eqs. (S13), (S16), and (S18) simultaneously.
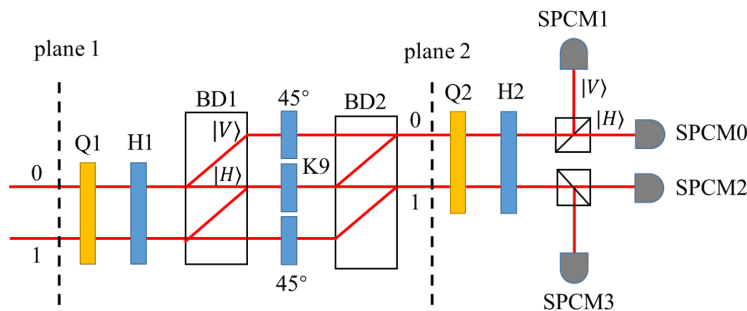
FIG. S3. The measurement module employed for the verification of the CNOT gate. The PAS in Fig. 2 in the main text is unfolded here to better illustrate the structure of the measurement module.

C. Implementation of local projective measurements on a two-qubit system

Here we show that the measurement module employed for the verification of the CNOT gate shown in Fig. 2 in the main text as reproduced in Fig. S3 can realize arbitrary local projective measurements on the output two-qubit state of the quantum-gate module.

Suppose we want to perform projective measurements onto orthonormal bases $\{|\varphi_0^{(0)}\rangle, |\varphi_1^{(0)}\rangle\}$ and $\{|\varphi_0^{(1)}\rangle, |\varphi_1^{(1)}\rangle\}$ for the path qubit and polarization qubit, respectively. To simplify the notation, here we temporarily use $|0\rangle$ ($|1\rangle$) to refer to "horizontal polarization" ("vertical polarization") for the polarization qubit. Suppose the photon state at plane 1 has the form

$$|\Psi\rangle = \sum_{i,j\in\{0,1\}} a_{ij}|\varphi_i^{(0)}\rangle|\varphi_j^{(1)}\rangle. \tag{S19}$$

We first choose the angles of the optical axes of Q1 and H1 in Fig. S3 so as to implement the transformation $|\varphi_0^{(1)}\rangle \to |0\rangle$, $|\varphi_1^{(1)}\rangle \to |1\rangle$ on the polarization qubit (see the Supplemental Material of Ref. [3] on how to calculate the angles), which turns $|\Psi\rangle$ into

$$|\Psi'\rangle = \sum_{i,j\in\{0,1\}} a_{ij}|\varphi_i^{(0)}\rangle|j\rangle. \tag{S20}$$

Then the two BDs split and re-combine the two light beams, which turns $|\Psi'\rangle$ into

$$|\Psi''\rangle = \sum_{i,j\in\{0,1\}} a_{j(1-i)}|i\rangle|\varphi_j^{(0)}\rangle \tag{S21}$$

at plane 2.

Next, we set the angles of the optical axes of Q2 and H2 so as to realize the transformation $|\varphi_0^{(0)}\rangle \to |0\rangle$, $|\varphi_1^{(0)}\rangle \to |1\rangle$, which turns $|\Psi''\rangle$ into

$$|\Psi'''\rangle = \sum_{i,j\in\{0,1\}} a_{j(1-i)}|i\rangle|j\rangle. \tag{S22}$$

Now, the probabilities that the heralded photon is detected by SPCM 0 to 3 are given by $|a_{01}|^2$, $|a_{11}|^2$, $|a_{00}|^2$, $|a_{10}|^2$, respectively. In this way, we can realize the projective measurement onto the product basis

$$\left\{|\varphi_0^{(0)}\rangle|\varphi_0^{(1)}\rangle, |\varphi_0^{(0)}\rangle|\varphi_1^{(1)}\rangle, |\varphi_1^{(0)}\rangle|\varphi_0^{(1)}\rangle, |\varphi_1^{(0)}\rangle|\varphi_1^{(1)}\rangle\right\}. \tag{S23}$$
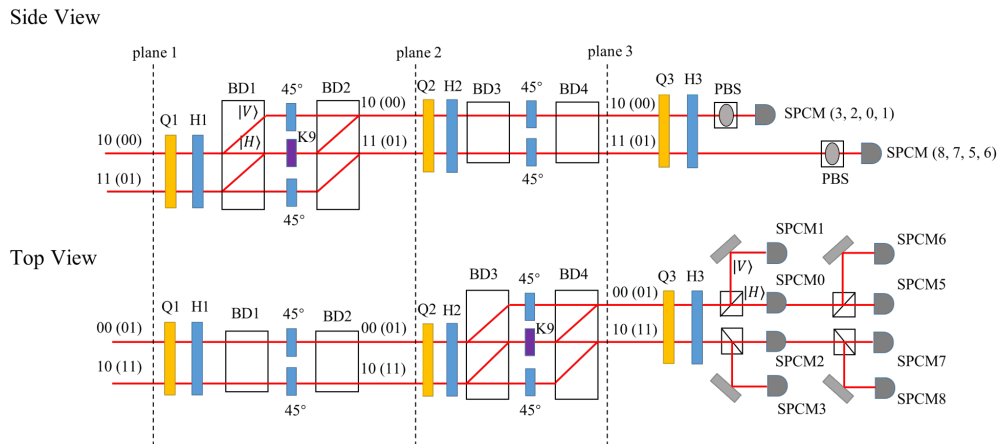
FIG. S4. The measurement module employed for the verification of the Toffoli gate. Since the trajectory of the photon cannot be described in a plane, we provide both the side view and the top view. The PAS in Fig. 2 in the main text is unfolded here to better illustrate the structure of the measurement module. The mirror right ahead of the PAS in Fig. 2 is removed in this figure.

D. Implementation of local projective measurements on a three-qubit system

Here we show that the measurement module employed for the verification of the Toffoli gate shown in Fig. 2 in the main text as reproduced in Fig. S4 can realize arbitrary local projective measurements on the output three-qubit states of the quantum-gate module.

Suppose we want to perform projective measurements onto the three orthonormal bases $\{|\psi_0^{(0)}\rangle, |\psi_1^{(0)}\rangle\}$, $\{|\psi_0^{(1)}\rangle, |\psi_1^{(1)}\rangle\}$, and $\{|\psi_0^{(2)}\rangle, |\psi_1^{(2)}\rangle\}$ for the two path qubits and one polarization qubit, respectively. To simplify the notation, here we temporarily use $|0\rangle$ ($|1\rangle$) to refer to "horizontal polarization" ("vertical polarization") for the polarization qubit. Suppose the photon state at plane 1 has the form

$$|\Psi_0\rangle = \sum_{i,j,k \in \{0,1\}} a_{ijk} |\psi_i^{(0)}\rangle |\psi_j^{(1)}\rangle |\psi_k^{(2)}\rangle. \tag{S24}$$

We first choose the angles of the optical axes of Q1 and H1 in Fig. S4 so as to implement the transformation $|\psi_0^{(2)}\rangle \to |0\rangle, |\psi_1^{(2)}\rangle \to |1\rangle$ on the polarization qubit, which turns $|\Psi_0\rangle$ into

$$|\Psi_1\rangle = \sum_{i,j,k \in \{0,1\}} a_{ijk} |\psi_i^{(0)}\rangle |\psi_j^{(1)}\rangle |k\rangle. \tag{S25}$$

Then BD1 and BD2 split and re-combine the two light beams, which turns $|\Psi_1\rangle$ into

$$|\Psi_2\rangle = \sum_{i,j,k \in \{0,1\}} a_{ik(1-j)} |\psi_i^{(0)}\rangle |j\rangle |\psi_k^{(1)}\rangle \tag{S26}$$

at plane 2.

Next, we set the angles of the optical axes of Q2 and H2 so as to realize the transformation $|\psi_0^{(1)}\rangle \to |0\rangle, |\psi_1^{(1)}\rangle \to |1\rangle$ on the polarization qubit, which turns $|\Psi_2\rangle$ into

$$|\Psi_3\rangle = \sum_{i,j,k \in \{0,1\}} a_{ik(1-j)} |\psi_i^{(0)}\rangle |j\rangle |k\rangle. \tag{S27}$$

Then BD3 and BD4 split and re-combine the two light beams, which turns $|\Psi_3\rangle$ into

$$|\Psi_4\rangle = \sum_{i,j,k\in\{0,1\}} a_{k(1-j)(1-i)}|i\rangle|j\rangle|\psi_k^{(0)}\rangle \tag{S28}$$

at plane 3.

Finally, we set the angles of the optical axes of Q3 and H3 so as to realize the transformation $|\psi_0^{(0)}\rangle \to |0\rangle, |\psi_1^{(0)}\rangle \to |1\rangle$ on the polarization qubit, which turns $|\Psi_4\rangle$ into

$$|\Psi_5\rangle = \sum_{i,j,k\in\{0,1\}} a_{k(1-j)(1-i)}|i\rangle|j\rangle|k\rangle. \tag{S29}$$

Now, the probabilities that the heralded photon is detected by SPCMs 0 to 7 are given by $|a_{011}|^2$, $|a_{111}|^2$, $|a_{001}|^2$, $|a_{101}|^2$, $|a_{010}|^2$, $|a_{111}|^2$, $|a_{000}|^2$, $|a_{100}|^2$, respectively. In this way, we can realize the projective measurement onto the three-qubit product basis

$$\left\{ |\psi_0^{(0)}\rangle|\psi_0^{(1)}\rangle|\psi_0^{(2)}\rangle, \ |\psi_0^{(0)}\rangle|\psi_0^{(1)}\rangle|\psi_1^{(2)}\rangle, \ |\psi_0^{(0)}\rangle|\psi_1^{(1)}\rangle|\psi_0^{(2)}\rangle, \ |\psi_0^{(0)}\rangle|\psi_1^{(1)}\rangle|\psi_1^{(2)}\rangle, \right.$$
$$\left. |\psi_1^{(0)}\rangle|\psi_0^{(1)}\rangle|\psi_0^{(2)}\rangle, \ |\psi_1^{(0)}\rangle|\psi_0^{(1)}\rangle|\psi_1^{(2)}\rangle, \ |\psi_1^{(0)}\rangle|\psi_1^{(1)}\rangle|\psi_0^{(2)}\rangle, \ |\psi_1^{(0)}\rangle|\psi_1^{(1)}\rangle|\psi_1^{(2)}\rangle \right\}. \tag{S30}$$

S3. PROTOCOLS FOR VERIFYING THE CNOT AND TOFFOLI GATES

The procedure for constructing a verification protocol for a unitary transformation $\mathcal{U}$ consists of two steps [1, 4, 5]. First, we choose an ensemble of test states $\{\rho_j, p_j\}_j$, where each $\rho_j = |\psi_j\rangle\langle\psi_j|$ is a pure state and p_j is the probability of picking ρ_j. Next, we construct a verification strategy for each output state $\mathcal{U}(\rho_j)$ according to the framework of quantum state verification (QSV) [6]. A verification strategy for $\mathcal{U}(\rho_j)$ consists of a number of projective tests with test projectors $M_l^{(j)}$, which are chosen with probabilities $p_{l|j}$ given the test state ρ_j. The resulting verification operator for the state $\mathcal{U}(\rho_j)$ reads $\Omega_j = \sum_l p_{l|j} M_l^{(j)}$. By contrast, the process verification operator for $\mathcal{U}$ reads

$$\Theta := d\sum_j p_j \mathcal{U}^{-1}\left(\sum_l p_{l|j} M_l^{(j)}\right) \otimes \rho_j^* = d\sum_j p_j \mathcal{U}^{-1}(\Omega_j) \otimes \rho_j^*. \tag{S31}$$

When the set $\{\rho_j, p_j\}_j$ of test states is balanced, which means the condition $\sum_j p_j \rho_j = \mathbb{1}/d$ holds, the efficiency of the verification protocol is mainly determined by the spectral gap $\nu(\Theta)$ as shown in Eq. (5) in the main text. A larger spectral gap usually means a higher efficiency.

TABLE S1. Test states for the verification of the CNOT gate. Here $|H\rangle$ and $|V\rangle$ denote the eigenstates of Z with eigenvalues 1 and -1, respectively; $|D\rangle, |A\rangle, |R\rangle, |L\rangle$ are defined as $|D\rangle = \frac{|H\rangle+|V\rangle}{\sqrt{2}}$, $|A\rangle = \frac{|H\rangle-|V\rangle}{\sqrt{2}}$, $|R\rangle = \frac{|H\rangle+\mathrm{i}|V\rangle}{\sqrt{2}}$, $|L\rangle = \frac{|H\rangle-\mathrm{i}|V\rangle}{\sqrt{2}}$.

bases	states				index j
$Z \otimes Z$	$|HH\rangle$	$|HV\rangle$	$|VH\rangle$	$|VV\rangle$	$1 \sim 4$
$X \otimes X$	$|DD\rangle$	$|DA\rangle$	$|AD\rangle$	$|AA\rangle$	$5 \sim 8$
$Y \otimes Y$	$|RR\rangle$	$|RL\rangle$	$|LR\rangle$	$|LL\rangle$	$9 \sim 12$

A. Verification protocol for the CNOT gate

The matrix representation of the CNOT gate in the computational basis is

$$CX = \begin{bmatrix} 1 & 0 & 0 & 0 \\ 0 & 1 & 0 & 0 \\ 0 & 0 & 0 & 1 \\ 0 & 0 & 1 & 0 \end{bmatrix}. \tag{S32}$$

As test states, we choose the product eigenstates of the Pauli operators $Z \otimes Z$, $X \otimes X$, and $Y \otimes Y$, and each of them is selected with an equal probability of $1/12$. These test states are labeled as $|\psi_j\rangle, j = 1, ..., 12$, where the correspondence between the index j and the test state is shown in Table S1.

After the action of the CNOT gate, each ideal output state $CX|\psi_j\rangle$ for $j = 1, ..., 8$ is a product state and an eigenstate of a Pauli operator, and so can be verified by one measurement setting based on a Pauli measurement; the corresponding verification operator coincides with the projector onto $CX|\psi_j\rangle$, that is,

$$\Omega_j = CX|\psi_j\rangle\langle\psi_j|CX^\dagger, \quad j = 1, ..., 8. \tag{S33}$$

By contrast, each ideal output state $CX|\psi_j\rangle$ for $j = 9, ..., 12$ is a Bell state and can be verified by three measurement settings based on Pauli measurements [6]. To be specific, the verification operator Ω_j has the form

$$\Omega_j = \frac{1}{3}\left(P^+_{(-1)^{b_0+b_1+1}XZ} + P^+_{(-1)^{b_1}YX} + P^+_{(-1)^{b_0}ZY}\right) = \frac{1}{3}\left(2CX|\psi_j\rangle\langle\psi_j|CX^\dagger + \mathbb{1}\right), \quad j = 9, ..., 12, \tag{S34}$$

where b_1b_0 is the binary representation of the number $j - 9$, and $P^+_{O_1O_2}$ denotes the projector onto the eigenspace of $O_1 \otimes O_2$ associated with eigenvalue 1. The spectral gap of the resulting process verification operator Θ reads

$$\nu(\Theta) = \frac{5}{9}. \tag{S35}$$

TABLE S2. Test states for the verification of the Toffoli gate. Here $|H\rangle$ and $|V\rangle$ denote the eigenstates of Z with eigenvalues 1 and -1, respectively; $|D\rangle, |A\rangle$ are defined as $|D\rangle = \frac{|H\rangle+|V\rangle}{\sqrt{2}}$, $|A\rangle = \frac{|H\rangle-|V\rangle}{\sqrt{2}}$.

bases	states								index j
$Z \otimes Z \otimes X$	$|HHD\rangle$	$|HHA\rangle$	$|HVD\rangle$	$|HVA\rangle$	$|VHD\rangle$	$|VHA\rangle$	$|VVD\rangle$	$|VVA\rangle$	$1 \sim 8$
$X \otimes X \otimes Z$	$|DDH\rangle$	$|DDV\rangle$	$|DAH\rangle$	$|DAV\rangle$	$|ADH\rangle$	$|ADV\rangle$	$|AAH\rangle$	$|AAV\rangle$	$9 \sim 16$

B. Verification protocol for the Toffoli gate

The matrix representation of the Toffoli gate in the computational bases is

$$C^2X = \begin{bmatrix} 1 & 0 & 0 & 0 & 0 & 0 & 0 & 0 \\ 0 & 1 & 0 & 0 & 0 & 0 & 0 & 0 \\ 0 & 0 & 1 & 0 & 0 & 0 & 0 & 0 \\ 0 & 0 & 0 & 1 & 0 & 0 & 0 & 0 \\ 0 & 0 & 0 & 0 & 1 & 0 & 0 & 0 \\ 0 & 0 & 0 & 0 & 0 & 1 & 0 & 0 \\ 0 & 0 & 0 & 0 & 0 & 0 & 0 & 1 \\ 0 & 0 & 0 & 0 & 0 & 0 & 1 & 0 \end{bmatrix}. \tag{S36}$$

As test states, we choose the product eigenstates of the Pauli operators $Z \otimes Z \otimes X$ and $X \otimes X \otimes Z$, and each of them is selected with an equal probability of $1/16$. These test states are labeled as $|\psi_j\rangle, j = 1, ..., 16$, where the correspondence between the index j and the test state is shown in Table S2.

After the action of the Toffoli gate, each ideal output state $C^2X|\psi_j\rangle$ for $j = 1, ..., 8$ is still a product state and an eigenstate of a Pauli operator and so can be verified by one measurement setting based on a Pauli measurement; the resulting verification operator coincides with the projector onto $C^2X|\psi_j\rangle$, that is,

$$\Omega_j = C^2X|\psi_j\rangle\langle\psi_j|(C^2X)^\dagger, \quad j = 1, ..., 8. \tag{S37}$$

By contrast, each ideal output state $C^2X|\psi_j\rangle$ for $j = 9, ..., 16$ is a three-qubit hypergraph state up to some local unitary transformation and can be verified by a variant of the cover protocol proposed in Ref. [6]. To be specific, the verification strategy consists of three tests based on Pauli measurements chosen with probability $1/3$ each. The resulting verification operator reads

$$\Omega_j = \frac{1}{3} \left[f_1((-1)^{b_2}X, Z, X) + f_2(Z, (-1)^{b_1}X, X) + f_3(Z, Z, (-1)^{b_0}Z) \right], \quad j = 9, ..., 16, \tag{S38}$$

where $b_2 b_1 b_0$ is the binary representation of the number $j - 9$. Each test operation in Eq. (S38) has the form

$$f_k(O_1, O_2, O_3) := |O_k^+\rangle\langle O_k^+| \otimes \left(\mathbb{1} - |O_s^- O_t^-\rangle\langle O_s^- O_t^-| \right) + |O_k^-\rangle\langle O_k^-| \otimes |O_s^- O_t^-\rangle\langle O_s^- O_t^-|, \tag{S39}$$

where $k, s, t \in \{1, 2, 3\}$ are different from each other, O_i for $i = 1, 2, 3$ are Hermitian operators acting on the ith qubit, and $|O_i^+\rangle$ ($|O_i^-\rangle$) is the eigenstate of O_i with eigenvalue 1 (-1). The test $f_k(O_1, O_2, O_3)$ can be realized as follows: measure O_1, O_2, and O_3 on the three qubits, respectively, and accept the state if either (a) the measurement result on the kth qubit is 1 and the measurement results on the other two qubits are not $\{-1, -1\}$; or (b) the measurement result on the kth qubit is -1 and the measurement results on the other two qubits are $\{-1, -1\}$. The spectral gap of the resulting process verification operator Θ reads

$$\nu(\Theta) = \frac{1}{6}. \tag{S40}$$

S4. INFIDELITY ESTIMATION OF THE CNOT GATE AND THE TOFFOLI GATE

To understand the large-sample limit of practical QGV, we also perform QGV of the CNOT gate with 10^5 tests and QGV of the Toffoli gate with 5×10^5 tests. Equation (7) in the main text
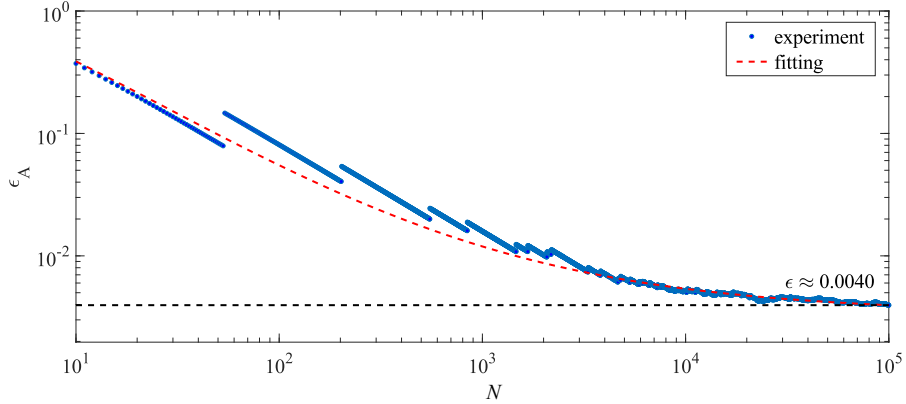
FIG. S5. Infidelity estimation of the CNOT gate based on QGV. Here the confidence level $1 - \delta$ is set to be 95%.
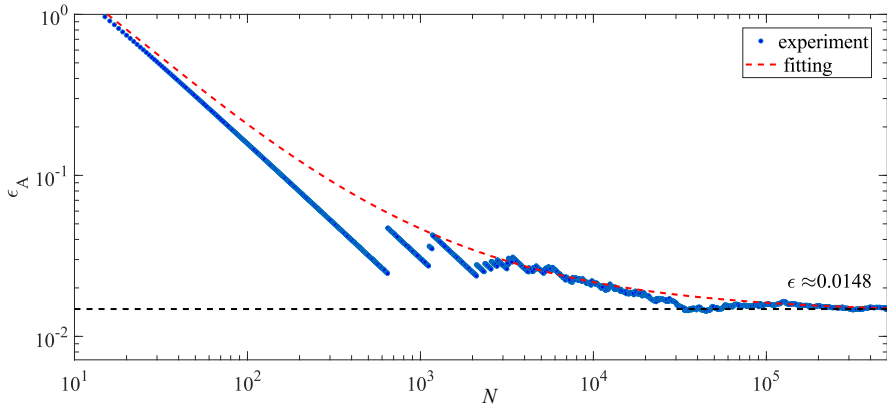
FIG. S6. Infidelity estimation of the Toffoli gate based on QGV. Here the confidence level $1 - \delta$ is set to be 95%.

is employed to estimate (upper bounds for) the infidelities of the two quantum gates, and the results are shown in Figs. S5 and S6, respectively. The infidelity of the CNOT gate converges to 0.004 after 10^5 tests, which is quite close to the result 0.003 determined by QPT. The infidelity of the Toffoli gate converges to 0.015 after 2×10^5 tests.

S5. PROCESS TOMOGRAPHY OF THE CNOT GATE

To determine the actual average gate fidelity of the CNOT gate, we perform QPT on the CNOT gate. Here we employ 36 probe states from the set $\{|H\rangle, |V\rangle, |D\rangle, |A\rangle, |R\rangle, |L\rangle\}^{\otimes 2}$ and all 9 Pauli measurement settings. In each experimental setting (which means a specific combination of a probe state and a measurement setting), we perform 20000 measurements in total (the large number of measurements are employed to suppress the statistical fluctuation). Then the
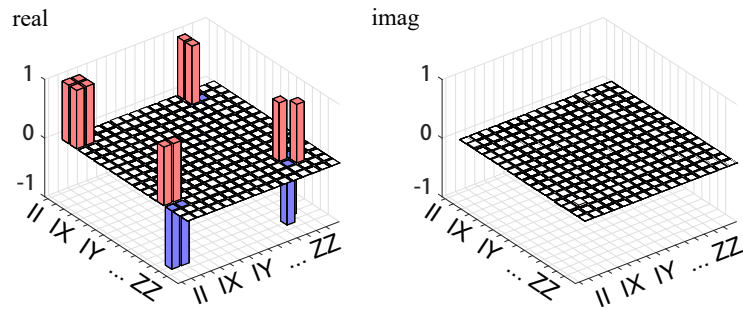
FIG. S7. The result of QPT of the CNOT gate. Here "real" and "imag" denote the real and imaginary parts, respectively. Bars without color represent the ideal CNOT gate, while bars with color represent the actual CNOT gate. The average gate fidelity of the CNOT gate is $F_A = 0.997$.

maximum likelihood method is employed to infer the process matrix of the CNOT gate from the measurement data [7]. The result of QPT is shown in Fig. S7, from which we can determine the average gate fidelity of the CNOT gate, with the result 0.997.

[1] H. Zhu and H. Zhang, Phys. Rev. A **101**, 042316 (2020).
[2] A. Dimić and B. Dakić, npj Quantum Inf. **4**, 11 (2018).
[3] Z. Hou, H. Zhu, G. Y. Xiang, C. F. Li, and G. C. Guo, J. Opt. Soc. Am. B **33**, 1256 (2016).
[4] Y.-C. Liu, J. Shang, X.-D. Yu, and X. Zhang, Phys. Rev. A **101**, 042315 (2020).
[5] P. Zeng, Y. Zhou, and Z. Liu, Phys. Rev. Research **2**, 023306 (2020).
[6] S. Pallister, N. Linden, and A. Montanaro, Phys. Rev. Lett. **120**, 170502 (2018).
[7] M. Ježek, J. Fiurášek, and Z. Hradil, Phys. Rev. A **68**, 012305 (2003).